Advances in Geo-Energy Research

Vol. 19, No. 2, p. 118-130, 2026

Original article

Optical characterization of full-field deformation and damage evolution in hot dry rock under mechanical loading

Fatick Nath[1,2]*, Rene Garcilazo Jr.[1,2], Eleazar Rojas Cabezudo[1]

[1]*Petroleum Engineering Program, Texas A&M International University, Laredo 78041, USA*

[2]*Geomechanics for Geo-Energy and Geo-Storage (G3) Laboratory, School of Engineering, Texas A&M International University, Laredo 78041, USA*

Keywords:
Enhanced geothermal systems
three-dimensional digital image correlation
damage variables
uniaxial compression test
diametrical compression test

Cited as:
Nath, F., Garcilazo Jr., R., Cabezudo, E. R. Optical characterization of full-field deformation and damage evolution in hot dry rock under mechanical loading. Advances in Geo-Energy Research, 2026, 19(2): 118-130.
https://doi.org/10.46690/ager.2026.02.02

Abstract:
Geothermal energy continues to emerge as a reliable, low-carbon resource with strong potential to support long-term clean energy goals. However, the development of enhanced geothermal systems is often limited by incomplete understanding of fracture initiation, propagation, and associated damage evolution within hot dry rock. Accurately characterizing these processes is essential for predicting stimulation outcomes and ensuring reservoir stability. This study employs high-resolution three-dimensional digital image correlation (DIC) to quantify strain localization and damage progression in hot dry rock samples collected from the Department of Energy Utah FORGE project's Well 16B (78)-32. Laboratory tests conducted under uniaxial compression and Brazilian tensile loading provide a controlled framework for observing mechanical responses under contrasting stress regimes. The DIC-based analysis identifies four distinct deformation stages: Initial closure, linear elastic response, elastic-plastic transition, and a final plastic phase associated with unstable fracture growth. Across both loading conditions, deformation is governed by tensile-dominated strain fields, with fractures consistently initiating and propagating along the specimen centerline. Damage variables derived from strain statistics range from approximately $0.25 \pm 10\%$ in Brazilian tensile tests to $0.30 \pm 20\%$ in uniaxial compression, with all samples falling within a broader interval of 0.25 to 0.40. These values reflect meaningful variations in internal degradation influenced by loading mode and specimen geometry. Overall, the findings advance the fundamental understanding of hot dry rock fracture mechanics and provide quantitative parameters that can enhance geomechanical modeling, improve stimulation design, and contribute to more effective and reliable geothermal reservoir development.

1. Introduction

Geothermal energy is increasingly recognized as a reliable and environmentally responsible alternative to fossil fuels. Unlike intermittent renewables, geothermal systems can provide continuous baseload power, and even a small fraction of the Earth's geothermal heat could meet global energy demand for extraordinarily long timescales (Diamandis and Rose-Washington, 2023; Horne et al., 2025; Huenges et al., 2025). Within this broader energy landscape, hot dry rock (HDR) formations are particularly attractive because of their vast heat content, widespread distribution, and suitability for large-scale deployment, making them central to the future development of enhanced geothermal systems (EGS).

EGS unlocks this heat by injecting fluids into deep, hot, low-permeability rocks and circulating them through engineered fracture networks. As the fluid moves through the rock, it absorbs heat and returns to the surface for power generation

Yandy Scientific Press

*Corresponding author.
E-mail address: fatick.nath@tamiu.edu (F. Nath); renegarcilazo@dusty.tamiu.edu (R. Garcilazo Jr.); eleazarcabezudo4@gmail.com (E. R. Cabezudo).

Received November 2, 2025; revised December 14, 2025; accepted January 9, 2026; available online January 13, 2026.

Fig. 1. Location map of the Utah FORGE geothermal field showing the orientation and spatial distribution of wells, including Well 16B (78)-32, from which the HDR samples used in this study were collected for laboratory mechanical testing (Utah FORGE, 2025).

or direct-use applications (Xia et al., 2017; Fleckenstein et al., 2022). The success of this process, however, hinges on a delicate balance: Stimulation must enhance permeability sufficiently to sustain circulation, yet excessive deformation or fracture growth can compromise rock integrity and long-term reservoir performance. This balance is governed by how HDR deforms and accumulates damage under increasing stress.

During fluid injection, elevated pore pressure alters the *in-situ* stress state, promoting microcrack initiation and progressive deformation within the reservoir. While these processes are essential for creating connected flow paths, they can also weaken the rock framework, reduce reservoir lifespan, or trigger induced seismicity if damage becomes uncontrolled (Xie and Min, 2016; Simmons et al., 2019; Nadimi et al., 2020). A mechanistic understanding of how damage initiates, localizes, and evolves is therefore critical for designing safe and effective HDR stimulation strategies.

Deformation provides the earliest observable signal of this evolving mechanical state. As loading progresses, changes in stiffness and strength accompany the growth of microcracks, and strain begins to concentrate within localized zones (Xing et al., 2020). With continued stress, these zones interact and coalesce, ultimately forming macroscopic fractures that produce nonlinear stress-strain responses and progressive loss of load-bearing capacity (Amitrano, 2006; Luo et al., 2018). Capturing this transition from distributed microcracking to fracture-dominated failure is essential for predicting HDR reservoir behavior and avoiding over-stimulation.

Damage variables offer a practical way to describe this degradation by linking mechanical response to the progressive failure of material integrity. Originally developed within continuum damage mechanics, this concept provides a quantitative measure of how rock properties evolve under stress and has become a useful tool for assessing long-term stability in geosystems (Ni et al., 2009; Cui and Han, 2018). The challenge, however, lies in measuring damage in a way that reflects its true spatial complex heterogeneity.

Traditional techniques such as strain gauges or extensometers record deformation at only a few points, often missing where damage actually initiates. Three-dimensional digital image correlation (3D-DIC) overcomes this limitation by offering full-field, non-contact measurements of surface displacement and strain. By tracking changes in speckle patterns during loading, 3D-DIC reveals where strain localizes, how fractures initiate, and how damage evolves across the entire specimen (Pan et al., 2009). This makes it especially well-suited for studying the failure processes in geothermal rocks.

To date, most 3D-DIC studies have focused on sedimentary rocks such as sandstones and shales, where fracture patterns and strain localization have been well documented (Zhang et al., 2012; Rue, 2015; Munoz et al., 2016; Zhou et al., 2019). Other investigations have also contributed valuable insights into fracture evolution in rock-like materials (Zhang et al., 2012; Na et al., 2017; Chai et al., 2020). Its application to HDR, however, remains comparatively limited. Recent work on Utah FORGE granitic samples has demonstrated the promise of 3D-DIC for tracking deformation and estimating damage variables, but the coupling between stress, strain localization, and damage evolution in HDR systems is still not fully resolved (Nath et al., 2023; Nath and Cabezudo, 2024).

This study addresses that gap by applying 3D-DIC to systematically investigate damage development in HDR cores from the Department of Energy (DOE) Utah FORGE Well 16B(78)-32. Using unconfined compression and Brazilian disc tests, the evolution of strain, fracture initiation, and damage variables is tracked from initial loading through failure. By directly linking full-field deformation measurements with damage mechanics, this work provides new insight into how HDR failure occurred under stress. These insights help refine stimulation strategies, improve geothermal reservoir mechanical properties, and support the long-term viability of EGS as a cornerstone of a sustainable energy future.

2. Materials

This study collected potential HDR samples from well 16B (78)-32 of the DOE Utah FORGE project, located at depths between 8,508.1 and 8,508.7 feet, as indicated by an orange star on the FORGE site map (Fig. 1). This research examined HDR samples obtained from Utah FORGE well and the depths of the candidate sample between 8,508.3 and 8,508.5 feet. A portion of this sample was used for the preliminary analysis of deformation evolution (Nath et al., 2023) and the characterization of damage variables (Nath and Cabezudo, 2024).

Building on the preliminary understanding of HDR deformation behaviors, the study conducted an in-depth examination of deformation characteristics and damage variables. For this purpose, brazilian disc test (BDT) (ASTM D3967-08, 2008) and the unconfined compressive strength (UCS) test (ASTM D2938-95, 2017) were performed on a newly prepared sample derived from the obtained core samples. Table 1 presents the details of the candidate samples.

Petrographic and X-ray diffraction analyses of Utah FORGE cores reported by Jones et al. (2023) show that the granitic host rock is composed mainly of plagioclase, K-feldspar, and quartz, with minor biotite and hornblende. The

Table 1. HDR tested sample descriptions collected from 16B (78)-32.

No.	Core depth (ft)	Tested sample depth (ft)	Test type	Average dia (in)	Average length (in)	Weight (gm)	Bulk density (g/cm^3)	Average density (g/cm^3)
1	8,508.1-8,508.7	8,508.3-8,508.5	BDT	0.898	0.389	10.509	2.60	2.636
2	8,508.1-8,508.7	8,508.3-8,508.5	BDT	0.99	0.274	9.044	2.61	2.636
3	8,508.1-8,508.7	8,508.3-8,508.5	UCS	0.989	1.093	36.393	2.64	2.636
4	8,508.1-8,508.7	8,508.3-8,508.5	UCS	0.99	1.035	34.987	2.68	2.636

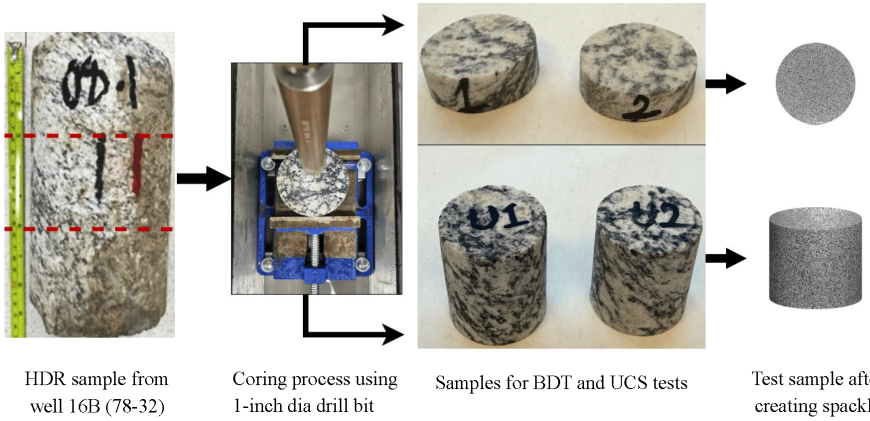

Fig. 2. Step-by-step sample preparation.

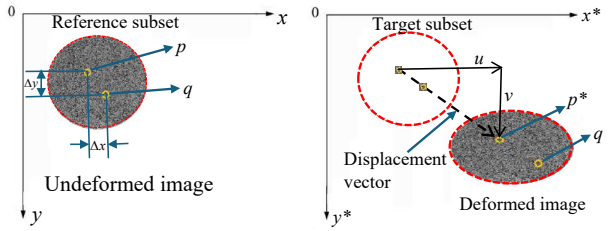

Fig. 3. DIC principle.

average bulk density of 2.60-2.65 g/cm^3 measured for the tested samples (Table 1) agrees with this mineral composition and reflects the crystalline nature of the formation. These characteristics explain the brittle behavior observed during uniaxial and diametrical compression tests and confirm that the tested specimens are representative of *in-situ* Utah FORGE material.

Prior to conducting the tests, we dried the samples for 24 h at 30 °C in an oven, in compliance with ASTM guidelines. After multiple steps for core specimen preparation, a black-on-white dot speckled pattern was prepared on the front face of the sample (toward the camera face of DIC system) by spraying using a skilled hand (Fig. 2).

3. Methods

3.1 Fundamentals of 3D-DIC

DIC is a non-destructive technique used to measure deformation fields in materials. It captures two-dimensional and three-dimensional displacement by comparing differences in gray levels between two digital images of the specimen's surface in different states. To determine displacement fields, DIC compares digital speckle images taken under various load conditions. The correlation coefficient is calculated through this method.

In Fig. 3, the coordinates of reference image (x,y) and deformed image (x^*,y^*) are mapped using a correlation function between the two images, where (p,p^*) and (q,q^*) represent the positions of the same point before and after deformation, respectively. In this process, u and v describe how each subset of the image shifts in the x- and y-directions, while the gradient terms $\partial u/\partial x$, $\partial u/\partial y$, $\partial v/\partial x$, $\partial v/\partial y$, capture the small strains and rotations that develop within the rock material. The local coordinates, Δx and Δy specify the position of each pixel relative to the center of the subset, allowing the algorithm to map how different parts of the subset deform. Distortion factors for the X direction are considered, and the average gray value of the reference image is denoted as $f(x,y)$, while the average gray value of the target image is represented as g (x^*,y^*). The correlation is based on comparing these average gray values between the reference and target images.

According to Zhang et al. (2012), the correlation coefficient can be computed using the following expression: This formulation follows the approach originally proposed by Pan et al. (2009) and has since been widely adopted in DIC analyses. The correlation values ranging from -1 (poor match) to 1 (perfect match):

$$c(X)=\frac{\sum_{i=1}^{m}\sum_{j=1}^{m}\left[f(x_i,y_j)-\bar{f}\right]\left[g(x_i^*,y_j^*)-\bar{g}\right]}{\sqrt{\sum_{i=1}^{m}\sum_{j=1}^{m}\left[f(x_i,y_j)-\bar{f}\right]^2\sum_{i=1}^{m}\sum_{j=1}^{m}\left[g(x_i^*,y_j^*)-\bar{g}\right]^2}} \quad (1)$$

$$X=\left(u,v,\frac{\partial u}{\partial x},\frac{\partial u}{\partial y},\frac{\partial v}{\partial x},\frac{\partial v}{\partial y}\right)$$

$$\begin{aligned} x^*&=x+u+\frac{\partial u}{\partial x}\Delta x+\frac{\partial u}{\partial y}\Delta y \\ y^*&=y+v+\frac{\partial v}{\partial x}\Delta x+\frac{\partial v}{\partial y}\Delta y \end{aligned} \quad (2)$$

The smoothness difference can also be used to measure strain using computer methods. The Langrangian strain equation (Sutton et al., 2009) is used to figure out the strain in the displacement gradient:

Horizontal strain:

$$\varepsilon_{xx}=\frac{\partial u}{\partial x}+\frac{1}{2}\left[\left(\frac{\partial u}{\partial x}\right)^2+\left(\frac{\partial v}{\partial x}\right)^2\right] \quad (3)$$

Vertical strain:

$$\varepsilon_{yy}=\frac{\partial u}{\partial y}+\frac{1}{2}\left[\left(\frac{\partial u}{\partial x}\right)^2+\left(\frac{\partial v}{\partial x}\right)^2\right] \quad (4)$$

Shear strain:

$$\varepsilon_{xy}=\frac{1}{2}\left(\frac{\partial u}{\partial y}+\frac{\partial v}{\partial x}\right)+\left(\frac{\partial u}{\partial x}\frac{\partial u}{\partial y}+\frac{\partial v}{\partial x}\frac{\partial v}{\partial y}\right) \quad (5)$$

3.2 Damage variables estimation from 3D-DIC strain map

Material degradation under stress is traditionally assessed by the reduction in load-bearing area. However, DIC offers a more precise method by analyzing strain distribution on the surface. DIC estimates damage through the standard deviation (S) of the principal strain and the maximum strain ($S_{\max}$) at the damage location, using specific points aligned with the fracture path (Chai et al., 2020; Xu et al., 2024).

The damage variable D is calculated as follows:

$$D=\frac{S}{S_{\max}} \quad (6)$$

Traditionally, damage is defined by the reduction in effective bearing area:

$$D=\frac{A_d}{A} \quad (7)$$

where A_d is the defect area, and A is the effective bearing area. This study modifies the damage variable by introducing the standard deviation of the principal strain (S), with $S_{\max}$ as the maximum strain at the damaged area. The standard deviation (S) is calculated as:

$$S=\sqrt{\frac{1}{n}\sum_{i=1}^{n}(X_i-\bar{X})^2} \quad (8)$$

where n is the number of statistical points, X_i is the principal strain at the i-th point, and $\bar{X}$ is the average principal strain along the measurement line. This value is calculated from the deformation map created by 3D-DIC.

3.3 Calibration of 3D-DIC setup and image acquisition

The Trilion 3D-DIC system used in this study includes a pair of FLIR Spinnaker cameras equipped with fixed-focus lenses, high-intensity blue-light illumination, and a dedicated data-acquisition computer. The setup captures synchronized images during rock compression, and all displacement and strain fields are processed using GOM Correlate software (Trilion, 2025).

During testing, the specimen fills the entire camera field of view, and image sequences are recorded continuously using the Trilion Snap system. The DIC analysis is performed by dividing the surface into small subsets that track how each region deforms throughout loading. A designated region of interest on the sample surface is used to extract detailed strain and displacement information. After the full sequence of images is collected, GOM Correlate performs the necessary calibration and computes the corresponding full-field deformation results.

Although only two or three frames are shown for clarity; the selected images represent the full temporal evolution of the deformation process. These stages were derived from analyzing the entire DIC dataset, ensuring that no intermediate mechanical behavior is omitted. Current study presents only the frames where distinguishable behavior occur, to avoid redundancy and maintain figure clarity. The strain field evolved gradually between these stages and was tracked alongside the load-displacement data in Figs. 5 and 6. Table 2 provides a structured summary of the system setup and calibration parameters based on best practice guidelines and used in our experiment.

3.4 Testing procedure

The HDR tests were performed on an Instron load frame under displacement control, with cameras synchronized to the loading system and the sample surface prepared with a black-and-white speckle pattern to enable accurate DIC measurements. The methods follow those outlined by Nath and Mokhtari (2018) and Aliabadian et al. (2019), Sharafisafa et al. (2020) and Nath et al. (2023), with DIC principles from Sutton et al. (2009) and Stirling et al. (2013). Fig. 4 illustrates the testing procedure.

Experiments were performed under laboratory temperature and pressure using uniaxial and diametral loading configurations to capture the deformation evolution of the HDR samples. These loading paths mimic the fundamental mechanical response relevant to multistage fracturing in EGS field settings. Although only two specimens were tested in each configuration due to limited core availability, both exhibited

Table 2. System and test parameters.

Parameter	Description
System	Two FLIR Spinnaker cameras, 50 mm fixed-focus lenses, blue-light sources, Trilion Snap Image-acquisition System
Camera	3-megapixel CMOS, 1,920 × 1,200 resolution
Capture rate	10 images per second
Software	GOM Correlate Professional for image processing; Bluehill Universal software for Instron load testing
Subset size	~25 pixels
Pixel spacing	~17 pixels
Pixel size	0.5 mm per pixel
Region of interest	40 mm × 80 mm
Field of view calibration resolution	< 0.04 μm/pixel (after 13 steps)
Compression test frame	100 kN Instron, 0.05 mm/min loading rate
Sampling rate	10 Hz
Synchronization	Cameras and Instron synchronized
Speckle pattern	Black-and-white speckles (~1 mm)

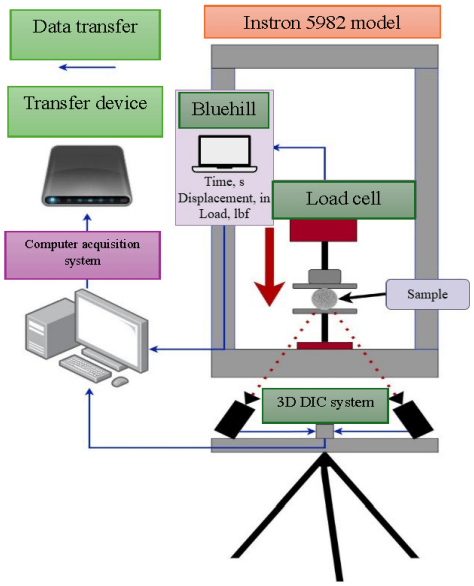

Fig. 4. Test set up employing 3D-DIC system.

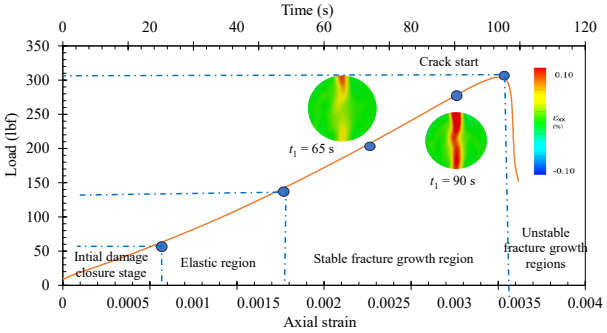

Fig. 5. Load-strain curve and DIC visualizations of Geothermal specimen during diametrical compression (BDT).

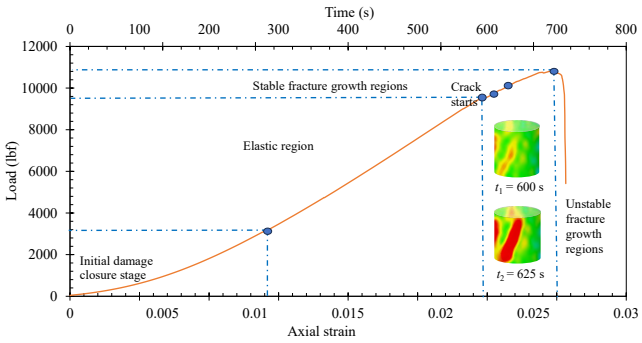

Fig. 6. Load-strain curve and DIC visualizations of Geothermal specimen during Uniaxial Compression (UCS).

consistent fracture orientations, strain-evolution patterns, and damage-variable trends, demonstrating reproducibility and minimizing variability related to sample count.

4. Results and analysis

4.1 Load vs. displacement characteristics in HDR

The preliminary analysis of damage, deformation, and fracture on HDR sample was conducted by Nath et al. (2023) and this study expanded by characterizing damage variables by Nath and Cabezudo (2024).

This research investigates damage and deformation in HDR samples from Utah FORGE well 16B (78)-32, using load-strain data from UCS and BDT analyses (Figs. 5 and 6). Brazilian tests showed pure tensile failure under diametrical compression, forming linked fractures due to increasing stress. BDT tests (Fig. 5) revealed failure due to pure tension under diametrical compression, highlighting the rock failure process

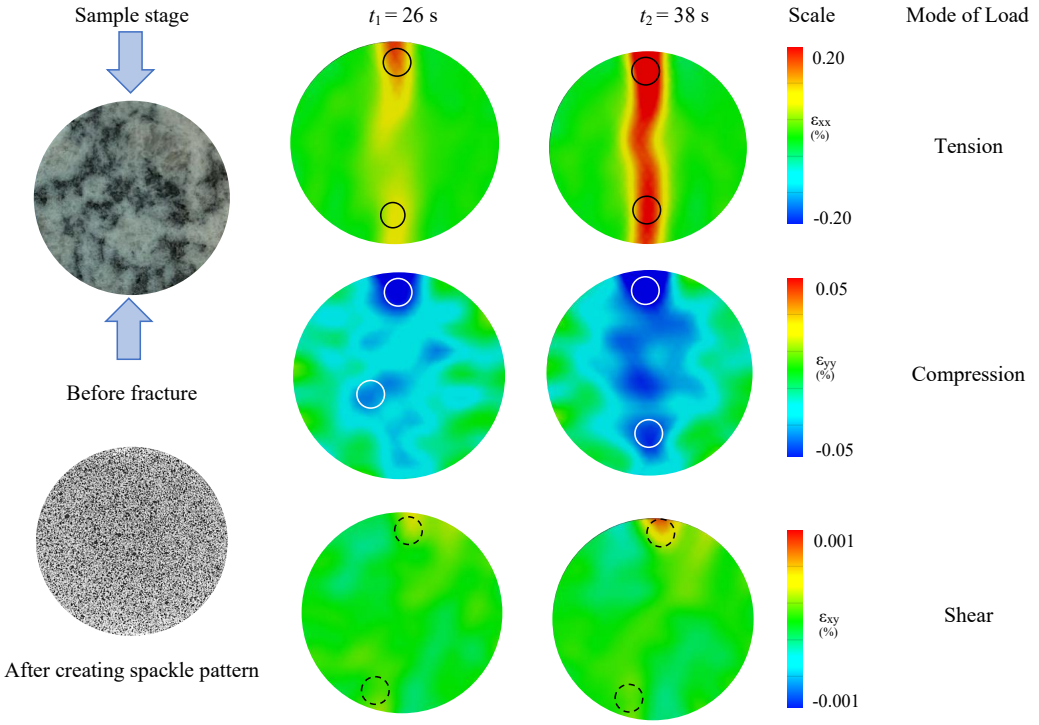

Fig. 7. Strain evolution (ε_{xx}, ε_{yy}, and ε_{xy}) during indirect tensile testing (BDT 1).

involving fracture initiation, propagation, interaction, and damage accumulation.

To better understand how the rock responds during uniaxial compression, the discussion first focuses on how strain begins to concentrate and how damage gradually builds throughout loading. As the load increases, the specimen moves through four recognizable stages: An initial response, a linear-elastic phase, a transition into elastic-plastic behavior, and finally a plastic stage where fractures become unstable. Fig. 6 visualizes this entire progression, showing how early loading triggers small internal breakdowns and compaction, which slightly reduce the rock's volume. With continued loading, these internal disturbances evolve into visible cracks that grow and eventually propagate rapidly, leading to unstable fractures and the final failure of the specimen.

4.2 Damage evolution on the HDR samples during BDT

A deformation evolution map illustrates the damage characteristics resulting from both diametrical and uniaxial compression using 3D-DIC. The deformation of the HDR sample is shown progressing in Fig. 7, which also includes shear (ε_{xy}), vertical (ε_{yy}), and horizontal (ε_{xx}) strain maps. A black circle (horizontal), a white circle (vertical), and a dotted black circle (shear) represent non-uniform variances.

These strain maps, which illustrate the onset and progression of fractures leading up to the samples' ultimate failure at various time steps (t_1, t_2), assist in identifying the types of failure and damage under compression, tension, or shear. Figs. 7 and 8 provide a detailed view of the damage characteristics under diametrical compression. As the radial load increases, strain develops along the midline of BDT samples #1 and #2, with strain accumulating at both ends (represented by black and white circles). In BDT 1, a straight central fracture begins to form as strain intensifies, while shear strain growth with increasing load is indicated by the dotted black circles.

The strain maps clearly show that pure tension is the primary failure mechanism for HDR samples. The variations in non-uniform displacement contours in Fig. 7 are likely to be due to the inherent variability of the HDR samples. In BDT 2, the diametrical load increases until it reaches the black circle, which marks the zone of maximum horizontal strain. As the compressive load continues, shear strain accumulates at the bottom loading end (dotted black circle), while vertical strain localizes at both ends (white circle). Fig. 8 further highlights the central failure pattern resulting from strain buildup, underscoring the tensile failure of the HDR sample under diametrical compression.

4.3 Damage evolution during uniaxial compression

During the UCS test, the HDR sample exhibits a clear buildup of strain along the vertical axis, accompanied by fracture growth that tends to follow the specimen's centerline. As the load increases, the strain field becomes increasingly dominated by tensile effects, guiding the direction and shape of the developing cracks. Figs. 9 and 10 depict this progression, capturing both the deformation pattern and the evolution of damage as the specimen approaches failure.

The negative strain (for ε_{xx}, ε_{yy}, and ε_{yy}) values represent localized compressive zones that naturally develop adjacent to areas undergoing tensile deformation. This behavior reflects

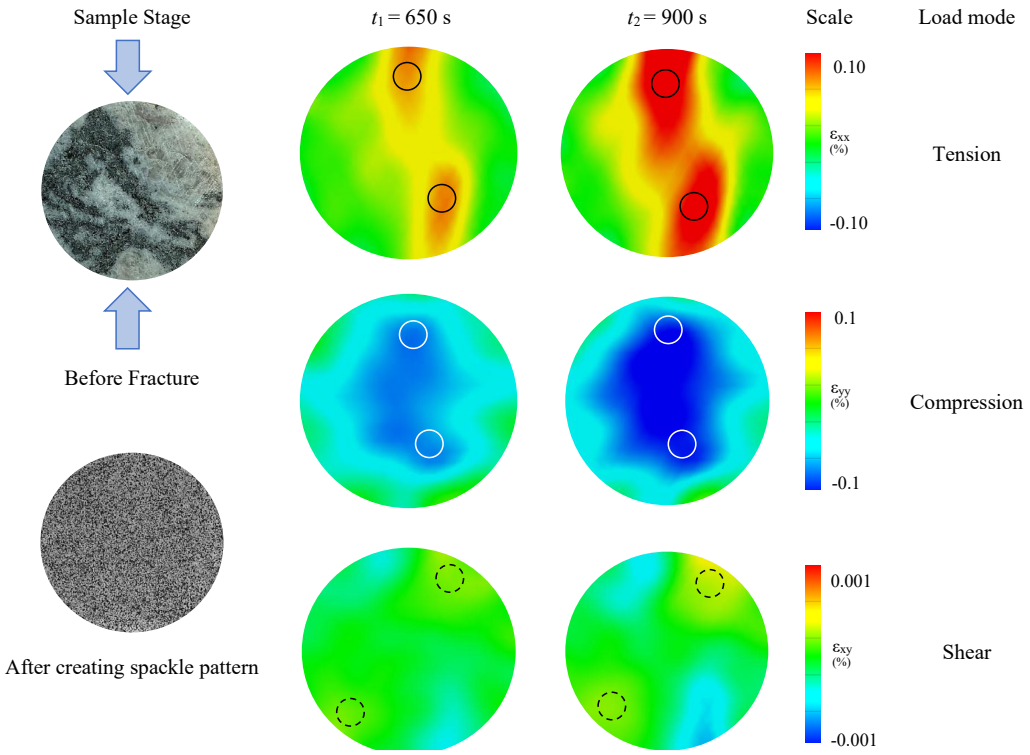

Fig. 8. Strain evolution (ε_{xx}, ε_{yy}, and ε_{xy}) during indirect tensile testing (BDT 2).

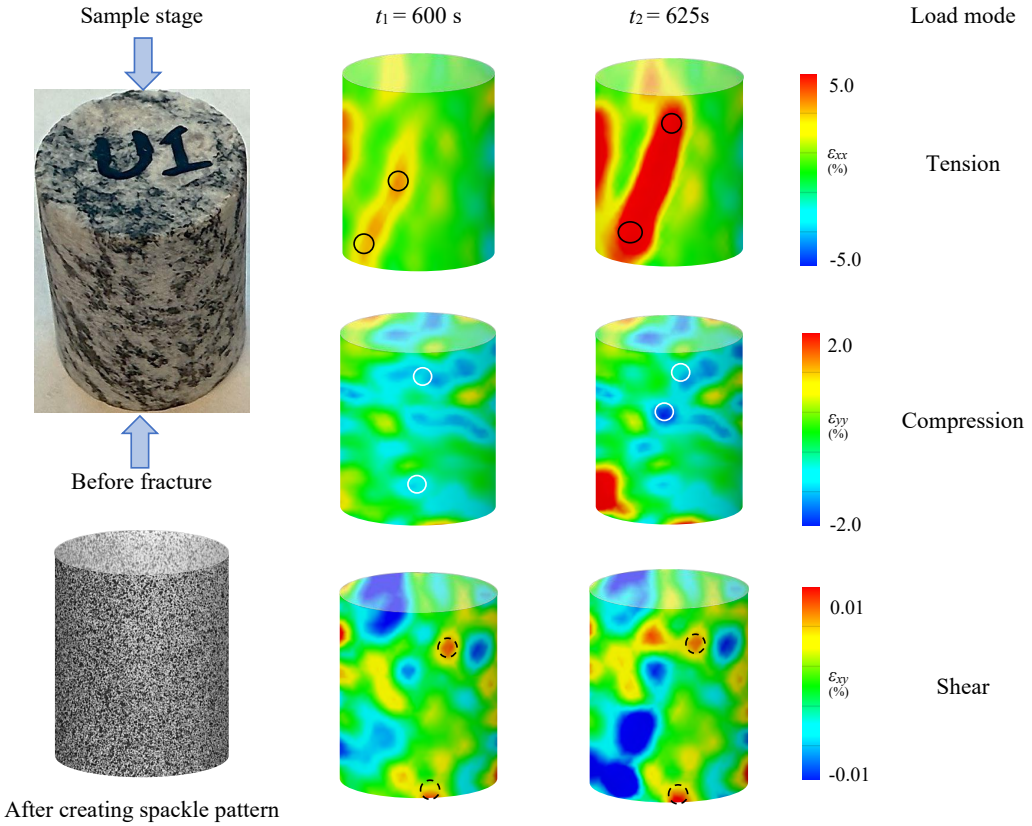

Fig. 9. Strain evolution (ε_{xx}, ε_{yy}, and ε_{xy}) during UCS 1 testing.

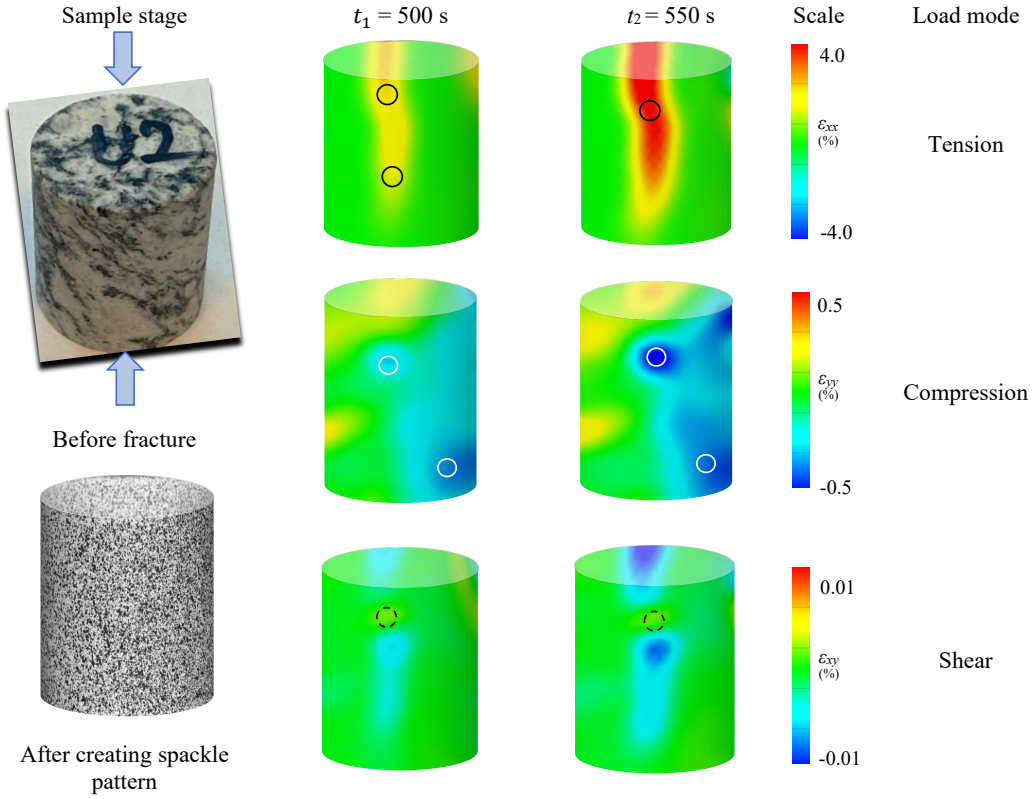

Fig. 10. Strain evolution (ε_{xx}, ε_{yy}, and ε_{xy}) during UCS 2 testing.

the stress redistribution that occurs prior to crack initiation, where portions of the sample experience lateral confinement or micro-compaction while neighboring regions accumulate tensile strain.

These negative strain regions are therefore not measurement artifacts, but a typical feature of mixed tensile-compressive interactions during the transitional stages leading up to tensile fracture.

Contrary to traditional assumptions, compression and shear are not the predominant failure mechanisms. Instead, the central fractures observed in all rock specimens confirm that pure tensile failure is the primary mechanism driving rock deformation under uniaxial compression conditions.

4.4 Damage variables

In rock mechanics, the damage variable quantifies internal material deterioration under stress. While traditionally estimated by reduced load-bearing area, DIC provides a more precise method. DIC measures surface strain distribution, enabling damage variable calculation using the standard deviation (S) of the major strain.

To quantify how damage develops within the rock, the analysis uses a measurement line placed across the DIC strain map, allowing the calculation of both the strain variability (S) and the maximum strain ($S_{\max}$). From these values, the damage variable is defined as the ratio $S/S_{\max}$, providing a simple way to track how strain becomes more uneven as the material deteriorates. This approach (illustrated in Fig. 11) was applied to BDT 1, BDT 2, UCS 1, and UCS 2 to examine damage progression along the ABCD line. The figure summarizes three key outputs: (a) the evolution of the damage variable, (b) changes in average maximum strain and strain standard deviation, and (c) the corresponding spatial distribution of damage on the DIC strain maps.

The damage variable calculation is organized into four stages-initial closure, linear elastic response, elastic-plastic damage, and finally plastic damage-based on how the strain field evolves in the DIC maps. This phased interpretation helps clarify the transition from early compaction to the onset of irreversible deformation. Fig. 12 illustrates this process by showing how the strain statistics change across these stages. Similar DIC-based statistical approaches have been used effectively in previous studies, including Chai et al. (2020) and Xu et al. (2024), to estimate damage variables with reasonable accuracy.

The synchronized rise of $\varepsilon_{x,\ \max}$ and $\varepsilon_{x,\ sigma}$ standard deviation in subfigures (b)-(c) mirrors the continuous increase in the damage variable shown in (a), confirming that strain heterogeneity with fracture evolution.

Initial damage progresses to micropore compaction, transitioning from internal to external changes. Visible damage occurs after this threshold. Damage variables, shown in Table 3, follow a consistent pattern, with BDT variables exceeding UCS values. The damage variables derived from DIC are estimated to be $0.25 \pm 10\%$ for the BDT and $0.3 \pm 20\%$ for UCS tests. Across all HDR samples, the damage variable ranges from 0.25 to 0.40, indicating internal microstructural degradation.

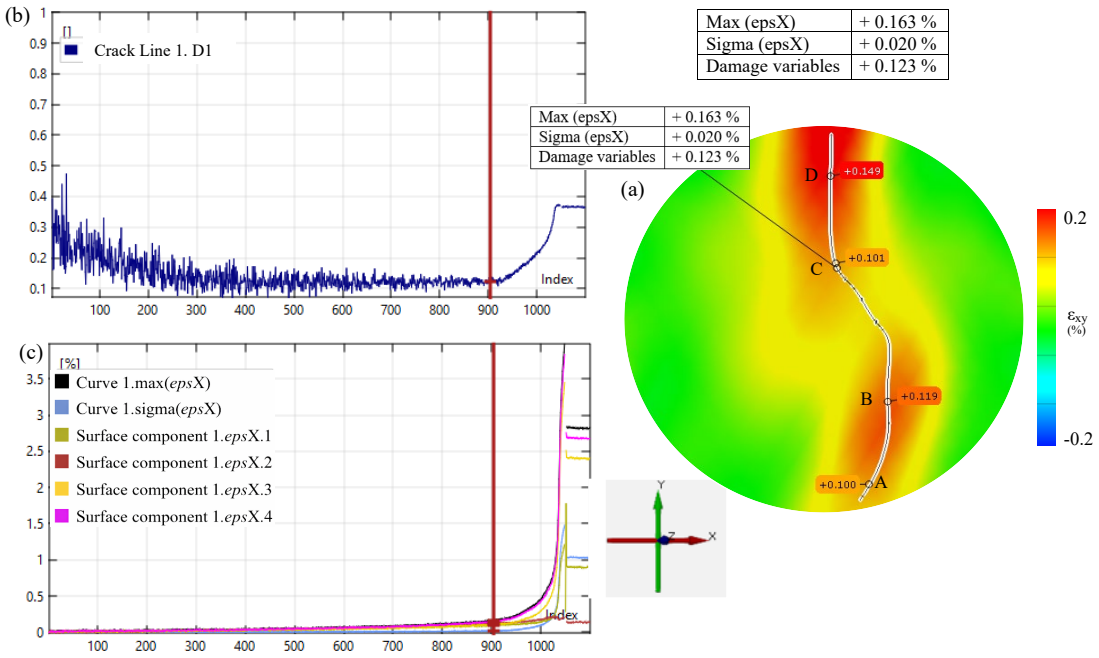

Fig. 11. Analysis of damage evolution in HDR along the drawn ABCD line-(a) evolution of the damage variable with loading steps, (b) variation of average maximum strain ($\varepsilon_{x,\ max}$) and standard deviation ($\varepsilon_{x,\ sigma}$) showing progressive increase with deformation along the ABCD line, and (c) corresponding DIC strain map indicating the spatial development of micro-fractures along ABCD. The coordinated evolution across (a)-(c) illustrates the real-time relationship between strain intensity and fracture propagation.

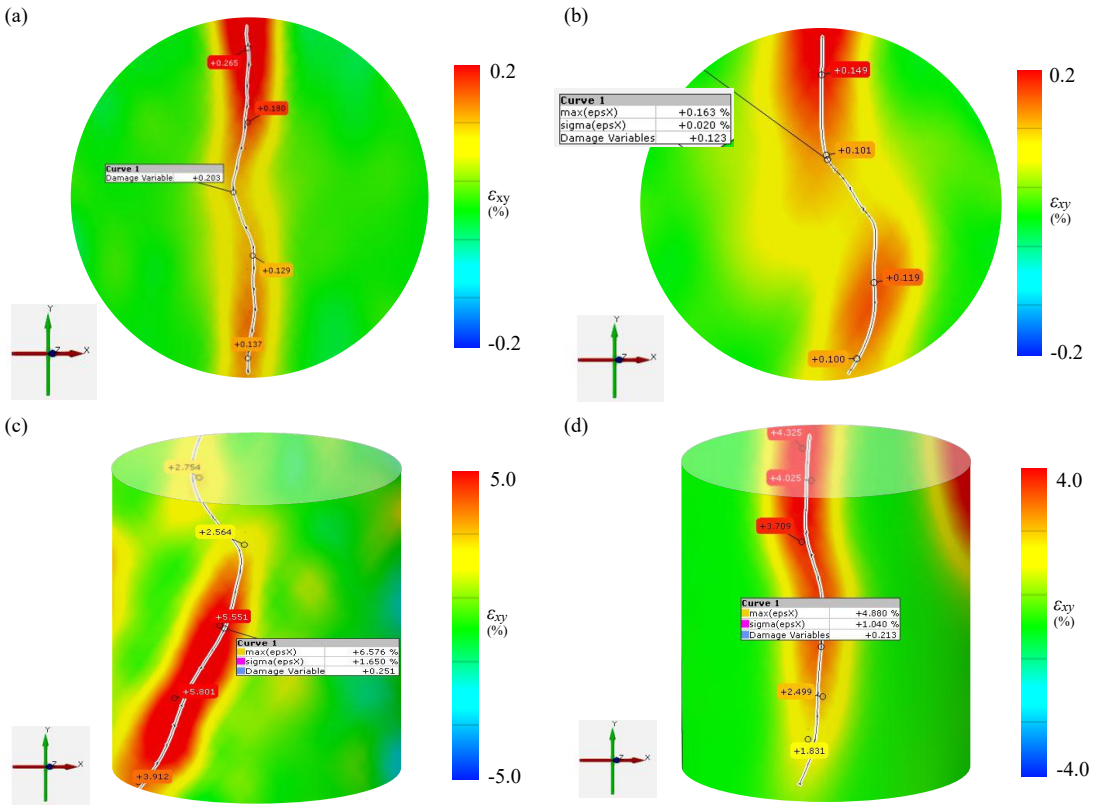

Fig. 12. Damage variable analysis along line ABCD for (a) BDT 1, (b) BDT 2, (c) UCS 1, and (d) UCS 2.

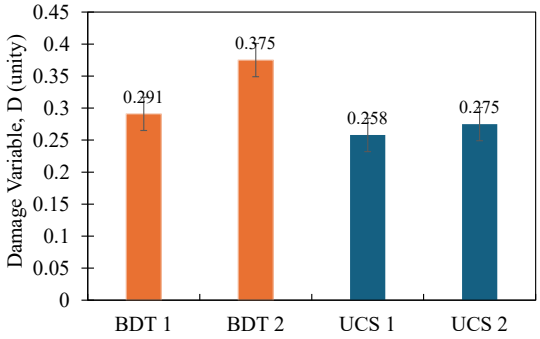

Fig. 13. Maximum stable damage variables observed in HDR samples damage variable analysis.

Table 3. Damage variable (D) of HDR during BDT and UCS.

Type	ε_{xx} (%)	D (unity)	D_{max}
BDT 1	0.11	0.15	0.291
	0.15	0.2	
	0.21	0.25	
	0.24	0.27	
	6.25	0.25	
BDT 2	0.163	0.123	0.375
	0.191	0.2	
	0.209	0.27	
	0.218	0.35	
	6.75	0.27	
UCS 1	2.5	0.15	0.258
	3.78	0.2	
	5.15	0.232	
	6.25	0.25	
UCS 2	2.15	0.15	0.275
	4.17	0.224	
	5.35	0.25	
	6.75	0.27	

The preliminary analysis of damage, deformation, and fracture in HDR samples was presented by the authors in Nath et al. (2023). This study was expanded by Nath and Cabezudo (2024) and further extended through the characterization of damage variables.

The maximum stable damage variables for the HDR samples were determined through the damage-variable analysis, revealing clear differences between the test configurations. The highest value ($D = 0.375$) was observed during the Brazilian tensile test (BDT 2), largely because this specimen had a slightly smaller thickness. This reduced thickness led BDT 2 to develop greater strain concentrations and a more pronounced tensile opening compared with BDT 1 under similar loading conditions. Fig. 13 presents these findings, highlighting how specimen geometry influences the onset and magnitude of damage accumulation.

4.5 Fracture pattern and failure mode

To analyze tensile strength variations, fracture patterns from BDT and UCS tests were examined. Table 4 categorizes these patterns as central or off-center central fractures. Notably, central fractures, observed across all specimens, indicate that tensile failure, rather than compression or shear, is the dominant failure mechanism under both uniaxial and diametral compression.

5. Discussions

5.1 Advanced fracture analysis using 3D-DIC in HDRs

3D-DIC has proven to be a powerful technique for analyzing the deformation and fracture behavior of HDR formations. It captures key features such as strain localization, stress concentration, and fracture initiation and growth. Unlike conventional strain-measurement methods, DIC provides a full-field, non-contact view of the entire sample surface, allowing direct visualization of crack evolution with high spatial resolution (Chai et al., 2020). It is important to note that the predominance of tensile failure observed here arises from low-confinement, room-temperature laboratory loading. Under *in-situ* EGS conditions involving higher confining pressures and thermal stresses, shear-slip mechanisms are expected to play a larger role.

Despite its precision, laboratory experiments cannot fully replicate the subsurface environment, where geothermal formations experience coupled with thermal, mechanical, and chemical effects (Na et al., 2017; Ma et al., 2018; Nath et al., 2023). Nevertheless, these controlled conditions provide valuable insight into the fundamental mechanical processes that govern deformation under EGS-like stress regimes. The tensile failure modes observed in this study are consistent with the low-confinement, room-temperature loading environment typical of laboratory DIC tests. In contrast, under *in-situ* EGS conditions, where higher confining pressure and temperature exist-slip mechanisms are expected to become more dominant.

5.2 Key considerations for DIC sample preparation and fracture mapping

Accurate DIC measurements depend strongly on meticulous sample preparation and system calibration. The surface must be well-polished, uniformly coated with a fine speckle pattern, and captured with properly aligned cameras to avoid distortion. Small imperfections can introduce noise, reduce correlation accuracy, or obscure fracture features (Chai et al., 2020).

Ideally, a homogeneous and isotropic rock should fracture symmetrically near the center under compression. However, the DIC strain maps in this study show deviations from this ideal behavior. These variations reflect the influence of miner-

Table 4. Fracture pattern of tested HDR samples.

Type	Fracture pattern	DIC schematic of fracture
BDT 1	Central fracture; Pure tensile failure	
BDT 2	Offset central fracture; tensile failure	
UCS 1	Offset central fracture; tensile failure	
UCS 2	Central fracture; Pure tensile failure	

al heterogeneity and anisotropy, which cause local strain concentrations and affect crack trajectories (Nath et al., 2023). Most Utah FORGE HDR samples displayed central tensile fractures, while one exhibited a slightly off-center failure-likely due to local mineral variability or microstructural irregularities. Such heterogeneity is inherent in crystalline geothermal rocks and must be considered when interpreting DIC data.

5.3 Mineralogical influence on fracture behavior

X-ray diffraction data from the Utah FORGE core (LLNL, 2023) reveal a mineralogical assemblage dominated by plagioclase, K-feldspar, and quartz, with accessory biotite, titanite, hornblende, apatite, and mixed-layer clays. The mechanical contrast between these minerals directly influences fracture patterns: Feldspars and quartz promote brittle failure, whereas clay minerals and biotite contribute to ductile deformation and anisotropy (Ma et al., 2018).

This mineralogical interplay explains the mixed fracture responses captured by DIC, where localized strain accumulations often follow mineral boundaries or cleavage planes. The observed patterns align with earlier studies on heterogeneous rocks, where fracture propagation was guided by mineral composition and grain-boundary interactions (Na et al., 2017; Nath et al., 2023). Understanding these microscale controls is essential for linking mineralogy to macroscopic damage evolution in HDR systems.

5.4 Environmental and engineering implications for geothermal applications

In real geothermal reservoirs, multiple environmental and operational factors influence fracture behavior and long-term performance. These include:

1) Thermal expansion and contraction under high-pressure, high-temperature conditions, which induce cyclic stress variations and accelerate crack propagation.
2) Reactive transport within pore spaces, where mineral dissolution and precipitation continuously alter permeability and fracture connectivity (Na et al., 2017).
3) Chemical-mechanical coupling, where injected fluids weaken mineral bonds and promote fracture linkage but can also cause secondary mineralization and sealing over time (Ma et al., 2018).

The interaction of these processes dictates reservoir evolution in EGS. While the present laboratory study isolates the mechanical component of deformation, it provides a foundational understanding of tensile-dominated fracture development. Future research should integrate thermal, mechanical, and chemical coupling, temperature-dependent tests, and cyclic loading analyses to simulate *in-situ* conditions more accurately.

A comprehensive understanding of long-term fracture stability, permeability evolution, and fluid-rock interactions will be essential for optimizing stimulation design and sustaining efficient geothermal energy extraction.

6. Conclusions

This study utilized 3D-DIC to investigate the deformation and damage evolution of HDR formations from the Utah FORGE site. The full-field, non-contact imaging capability of 3D-DIC enabled precise tracking of strain localization, fracture propagation, and microstructural degradation during loading. This optical approach provides a robust framework for evaluating fracture mechanics in geothermal materials and supports the development of predictive tools for EGS. Key findings are summarized as follows:

1) Damage Evolution Stages: Four sequential stages of deformation were identified-initial, linear elastic, elastic-plastic, and plastic damage. This progression confirms that HDR failure occurs in discrete steps, transitioning from stable deformation to unstable fracture growth.
2) Fracture Mechanisms: Experimental evidence shows that tensile failure dominates both uniaxial and diametral compression conditions. Central and near-central fractures in all specimens reveal that tension, rather than compression or shear, governs the primary deformation mode.
3) Damage Variable Quantification: Damage variables derived from 3D-DIC strain fields were estimated at $0.25 \pm 10\%$ for BDT and $0.30 \pm 20\%$ for UCS tests. Across all HDR samples, values between 0.25 and 0.40 indicate progressive internal degradation and confirm the sensitivity of DIC-based metrics for tracking microstructural damage.

These results advance the understanding of fracture mechanics in HDR systems and highlight 3D-DIC as an effective diagnostic tool for quantifying rock integrity under stress. By linking laboratory-scale optical measurements with macroscopic damage variables, this work lays the groundwork for physics-informed predictive modeling and improved geothermal reservoir management.

Future research should extend this framework to incorporate temperature-dependent deformation, cyclic loading, and chemical-mechanical coupling to better approximate *in-situ* EGS conditions. Integrating DIC data with geomechanical

simulations will further enhance the predictive capacity of damage-based models, ultimately guiding safer and more efficient geothermal energy extraction strategies.

Acknowledgements

The authors express gratitude to Texas A&M International University for funding their research through a start-up fund, TAMIU Presidential Award, and the university research development award, accelerating undergraduate studies in Geothermal Energy. The authors are also grateful to the US DOE Project, Utah FORGE, for providing HDR samples to conduct this research.

Conflicts of interest

The authors declare no competing interest.

References

Aliabadian, Z., Zhao, G. F., Russell, A. R. Failure, crack initiation and the tensile strength of transversely isotropic rock using the Brazilian test. International Journal of Rock Mechanics and Mining Sciences, 2019, 122: 104073.

Amitrano, D. Rupture by damage accumulation in rocks. International Journal of Fracture, 2006, 139: 369-380.

Advancing Standards transforming Markets, Standard test method for splitting tensile strength of intact rock core specimens. ASTM D3967-08, 2008.

Advancing Standards transforming Markets, Standard test method for unconfined compressive strength of intact rock core specimens. ASTM D2938-95, 2017.

Chai, J., Liu, Y., Yang, B., et al. Application of digital image correlation technique for the damage characteristic of rock-like specimens under uniaxial compression. Advances in Civil Engineering, 2020, 2020: 8857495.

Cui, Z., Han, W. *In situ* SEM observations of damage and crack growth of shale. Microscopy and Microanalysis, 2018, 24: 107-115.

Diamandis, P. H., Rose-Washington, C. Globally abundant cheap renewable energy, 2023.

Fleckenstein, W. W., Miskimins, J. L., Eustes, A. W., et al. Development of multi-stage fracturing system and wellbore tractor to enable zonal isolation during stimulation and EGS operations in horizontal wellbores. Paper SPE 210210 Presented at SPE Annual Technical Conference and Exhibition, Houston, Texas, 3-5 October, 2022.

Horne, R., Genter, A., McClure, M., et al. Enhanced geothermal systems for clean firm energy generation. Nature Reviews Clean Technology, 2025, 1: 148-160.

Huenges, E. Enhanced geothermal systems: Review and status of research and development. Geothermal Power Generation, 2025: 451-473.

Jones, C., Moore, J., Simmons, S. Utah FORGE: Well 16A(78)-32 core analysis results. Geothermal Data Repository, 2023.

Lawrence Livermore National Laboratory (LLNL). Utah FORGE: Powder X-ray diffraction data from well 16A(78)-32. LLNL, 2023.

Luo, Y., Xie, H., Ren, L., et al. Linear elastic fracture mechanics characterization of an anisotropic shale. Scientific Reports, 2018, 8: 8505.

Ma, T., Peng, N., Zhu, Z. Brazilian tensile strength of anisotropic rocks: Review and new insights. Energies, 2018, 11: 304.

Munoz, H., Taheri, A., et al. Pre-peak and post-peak rock strain characteristics during uniaxial compression by 3D digital image correlation. Rock Mechanics and Rock Engineering, 2016, 49(7): 2541-2554.

Na, S., Sun, W., Ingraham, M., et al. Effects of spatial heterogeneity and material anisotropy on fracture pattern and effective toughness of Mancos shale in Brazilian tests. Journal of Geophysical Research: Solid Earth, 2017, 122: 6202-6230.

Nadimi, S., Forbes, B., Moore, J., et al. Hydrogeothermal modeling of a granitic-based discrete fracture network for Utah FORGE. Geothermics, 2020, 87: 101853.

Nath, F., Cabezudo, E. Unraveling damage variables in hot dry rocks: An optical investigation of geothermal rocks from Utah FORGE. Paper SPE 221069 Presented at SPE Annual Technical Conference and Exhibition, New Orleans, Louisiana, 23-25 September, 2024.

Nath, F., Aguirre, G., Vazquez, E. C., et al. Deformation, damage, and fracture in hot dry rock under uniaxial and diametrical compression using 3D-DIC. Paper SPE 215048 Presented at SPE Annual Technical Conference and Exhibition, San Antonio, Texas, 16-18 October, 2023.

Nath, F., Mokhtari, M. Optical visualization of strain development and fracture propagation in laminated rocks. Journal of Petroleum Science and Engineering, 2018, 167: 354-365.

Ni, X., Zhu, Z., Zhao, J., et al. Meso-damage mechanical digitalization test of complete rock failure process. Rock and Soil Mechanics, 2009, 30: 3283-3290. (in Chinese)

Pan, B., Asundi, A., Xie, H., et al. Digital image correlation using iterative and pointwise least squares. Optics and Lasers in Engineering, 2009, 47: 865-874.

Rue, P. DIC: A revolution in experimental mechanics. Experimental Techniques, 2015, 39(6): 1-2.

Sharafisafa, M., Aliabadian, Z., Shen, L. Crack initiation and failure of block-in-matrix rocks under Brazilian test using digital image correlation. Theoretical and Applied Fracture Mechanics, 2020, 109: 102743.

Simmons, S. F., Kirby, S., Bartley, J., et al. Update on the geoscientific understanding of the Utah FORGE site. Paper SGP-TR-214 Presented at the 4th Workshop on Geothermal Reservoir Engineering, Stanford, California, 11-13 February, 2019.

Stirling, R. A., Simpson, D. J., Davie, C. T. Digital image correlation applied to Brazilian testing of sandstone. International Journal of Rock Mechanics and Mining Sciences, 2013, 60: 1-11.

Sutton, M. A., Orteu, J. J., Schreier, H. W. Image Correla-

tion for Shape, Motion, and Deformation Measurements. Springer, New York, USA, 2009.

Trilion. Digital image correlation. 2025.

Utah FORGE. Project data dashboard – Well data. Utah FORGE, 2025.

Xia, Y., Plummer, M., Mattson, E., et al. Design, modeling and evaluation of a doublet heat extraction model in EGS. Renewable Energy, 2017, 105: 232-247.

Xie, L., Min, K. B. Initiation and propagation of fracture shearing during hydraulic stimulation in EGS. Geothermics, 2016, 59: 107-120.

Xing, P., McLennan, J., Moore, J. *In-situ* stress measurements at the Utah FORGE site. Energies, 2020, 13(21): 5842.

Xu, M., Qi, X., Geng, D. Application of improved image repair algorithm in rock damage research. Scientific Reports, 2024, 14: 14849.

Zhang, H., Huang, G., Song, H., et al. Deformation and failure mechanisms under indentation using DIC. Engineering Fracture Mechanics, 2012, 96: 667-675.

Zhou, X. P., Wang, Y. T., et al. Fracturing behavior study of three-flawed specimens by uniaxial compression and 3D digital image correlation: Sensitivity to brittleness. Rock Mechanics and Rock Engineering, 2019, 52(3): 691-718.